Optics and Lasers in Engineering 50 (2012) 465–472

Contents lists available at SciVerse ScienceDirect

Optics and Lasers in Engineering

journal homepage: www.elsevier.com/locate/optlaseng

Characterization of the 3D resolution of topometric sensors based on fringe and speckle pattern projection by a 3D transfer function

Philipp Berssenbrügge [a,*], Markus Dekiff [a,1], Björn Kemper [b], Cornelia Denz [c,2], Dieter Dirksen [a,3]

[a] Department of Prosthetic Dentistry, University of Münster, Waldeyerstr. 30, 48149 Münster, Germany
[b] Center for Biomedical Optics and Photonics, University of Münster, Robert-Koch-Str. 45, 48129 Münster, Germany
[c] Institute of Applied Physics, University of Münster, Corrensstr. 2, 48149 Münster, Germany

ARTICLE INFO

Article history:
Received 1 September 2011
Received in revised form
11 October 2011
Accepted 15 October 2011
Available online 1 November 2011

Keywords:
Topometry
3D resolution
Modulation transfer function
Fringe projection
Speckle pattern correlation

ABSTRACT

The increasing importance of optical 3D measurement techniques and the growing number of available methods and systems require a fast and simple method to characterize the measurement accuracy. However, the conventional approach of comparing measured coordinates to known reference coordinates of a test target faces two major challenges: the precise fabrication of the target and – in case of pattern projecting systems – finding the position of the reference points in the obtained point cloud. The modulation transfer function (MTF) on the other hand is an established instrument to describe the resolution characteristics of 2D imaging systems. Here, the MTF concept is applied to two different topometric systems based on fringe and speckle pattern projection to obtain a 3D transfer function. We demonstrate that in the present case fringe projection provides typically 3.5 times the 3D resolution achieved with speckle pattern projection. By combining measurements of the 3D transfer function with 2D MTF measurements the dependency of 2D and 3D resolutions are characterized. We show that the method allows for a simple comparison of the 3D resolution of two 3D sensors using a low cost test target, which is easy to manufacture.

1. Introduction

The 3D acquisition of surfaces using optical topometry techniques like fringe or speckle pattern projection yields a point cloud containing a high quantity of coordinates that may be combined with colored textures to obtain a digital model of the regarded surface [1–5]. An overview of the recent development of fringe projection techniques and their applications is given in [6]. Various approaches to reduce measurement errors by dealing with different sources of error have been investigated. For example, quantization effects on the accuracy in the fringe projection case are discussed in [7]. This publication and [8] deal with an intensity correction of the projector to enhance accuracy. Systematic errors caused by image aberrations can either be corrected during camera calibration [9] or within the measurement process [10]. Lateral as well as depth depending lens distortions can be determined and reduced by an optimized lens design [11].

Thus, the determination of the measuring accuracy and its dependencies on various measurement conditions is a crucial point in many applications. However, it is still a challenging problem. One common method to determine accuracy is to use a groove plate as an test object [12]. This requires very precisely manufactured 3D structures in the test object. An overall error compensation method by comparing measured coordinates with those delivered by a coordinate measuring machine is presented in [13].

For a comparison of measured with reference coordinates in order to determine the accuracy, pairs of them have to be identified. This can either be done by picking the pixel positions of single target marks with known spatial distances manually or using a pattern recognition algorithm like an ellipse fit [14]. However, such an approach does not take into account the influence of pattern projection techniques. These methods are used for automated image analysis, e.g. in the topometric measuring systems described in Sections 2.2 and 2.3, and represent another accuracy limiting factor, which has to be considered. In these cases the locations of 3D points are obtained by analyzing the fringe or speckle pattern projected onto the surface under inspection. However, the acquired 3D points are not associated with features or marks of the surface itself. Thus, instead of

* Corresponding author. Tel.: +49 251 8343753; fax: +49 251 8347182.
E-mail addresses: berssenbruegge@uni-muenster.de (P. Berssenbrügge), markus.dekiff@uni-muenster.de (M. Dekiff), bkemper@uni-muenster.de (B. Kemper), denz@uni-muenster.de (C. Denz), dirksdi@uni-muenster.de (D. Dirksen).
[1] Tel.: +49 251 8347126; fax: +49 251 8347182.
[2] Tel.: +49 251 8333518; fax: +49 251 8339811.
[3] Tel.: +49 251 8356825; fax: +49 251 8347182.

0143-8166/$ - see front matter © 2011 Elsevier Ltd. All rights reserved.
doi:10.1016/j.optlaseng.2011.10.006

analyzing several single target marks for accuracy investigations, a more sophisticated technique has to evaluate features of the 3D model, which is given by the acquired point cloud. As a consequence, not the accuracy in terms of coordinate deviations, but a resolution of 3D structures is determined.

Goesele et al. [15] presented an approach for computing a 3D transfer function (3D TF) of a laser range scanner from a measurement of a test target containing a straight sharp edge. This was inspired by a slanted edge technique that estimates the MTF of 2D imaging systems [16]. In the present work we investigate whether this approach is suitable for a simple comparison of the 3D resolution of two different 3D sensors. First, the method is applied to a fringe projecting topometric sensor and combined with MTF measurements of the imaging systems involved in the topometric system. This allows for a direct comparison of 2D and 3D resolutions gained from the respective transfer functions. In order to compare the 3D resolutions of two types of pattern projection systems, we apply the same method to a second topometric sensor based on digital correlation of projected laser speckle patterns. Due to the monochromatic nature of laser light the latter approach offers the possibility of an effective reduction of ambient light by narrow-band filters and allows for a simple setup. Both systems use the same photogrammetric approach for calculating 3D coordinates. Thus the obtained results are highly comparable.

2. Theory and methods

2.1. Photogrammetry and calibration

The investigated topometric systems are based on the principle of photogrammetry, i.e. the calculation of 3D coordinates from images taken from different perspectives. Using the pinhole camera model, the mapping of the object coordinate (X, Y, Z) into the image plane is described in homogeneous coordinates [17] with an arbitrary scaling factor λ:

$$\lambda\begin{pmatrix} x \\ y \\ 1 \end{pmatrix} = \begin{pmatrix} fk_x & 0 & p_x \\ 0 & fk_y & p_y \\ 0 & 0 & 1 \end{pmatrix} R(I_3|-\mathbf{C}) \begin{pmatrix} X \\ Y \\ Z \\ 1 \end{pmatrix}, \tag{1}$$

where (x, y) denote the image coordinates, while the position and orientation of the camera in space are described by the translation vector $\mathbf{C}$ and the rotation matrix R. I_3 denotes the three-dimensional identity matrix. The pinhole model focal length f, which is the distance from the image plane to the camera center, is multiplied by the conversion factors k_x and k_y to obtain pixel coordinates along the x and y axes. (p_x, p_y) is the position of the principal point, i.e. the intersection of the optical axis and the image plane. In order to determine these parameters as well as additional lens distortion parameters [9], a calibration is performed following the approach of Zhang [18]. The advantages of this approach are its proven numerical stability and the possibility to use a plane field of target marks. Thus manufacturing problems associated with 3D structures are avoided. At least two images of the plane field in varied orientations have to be captured. From these images the imaging parameters are then estimated by a least-squares-fit.

After the setup has been calibrated, object coordinates can be calculated from at least two images of different perspectives. For this evaluation homologous image points, i.e. points in both images, which belong to the same object point [19], have to be identified. Subsequently, a system of equations for (X, Y, Z) has to be solved, which contains (1) for each perspective.

A special variant of two-camera photogrammetry is the stereo normal case. Here, the viewing directions are parallel to each other and perpendicular to the line which connects the two cameras (basis). It provides simple error formulas [20] for the measurement uncertainties σ_Z and σ_X of the coordinates Z (axial direction, (2)), X (3) and Y (analog formula to (3))

$$\sigma_Z = \frac{Z^2}{fb}\sigma_{p_x}, \tag{2}$$

$$\sigma_X = \sqrt{\left(\frac{x_1}{f}\frac{Z^2}{fb}\sigma_{p_x}\right)^2 + \left(\frac{Z}{f}\sigma_x\right)^2}, \tag{3}$$

where f denotes the focal length and b is the length of the basis. x_1 represents the corresponding x-coordinate of the first camera image and σ_{px} the uncertainty of the related parallax.

2.2. The fringe projecting topometric system

The topometric sensor investigated here is set up as depicted in Fig. 1. Two monochrome CCD cameras with digital interfaces (IEEE 1394) are used for image capturing, while fringe projection is performed by a video projector. The projector (Infocus) uses the DLP technology (Digital Light Processing) and has a pixel quantity of 1024×768. Cameras with pixel quantities of either 1024×768 or 1280×960 are employed. Fig. 1 also shows the test target used for the measurement of the 3D transfer function (see Section 2.5).

Phase measuring fringe projection [21] is applied to identify homologous image points automatically. For this purpose a sequence of seven Gray coded black-and-white and four sinusoidal vertical fringe patterns are projected onto the object and for each pattern an image is captured from two different perspectives. In combination with images of one completely white and one completely black projector illumination, binary values are calculated for each pixel from the seven black-and-white fringe pattern images. Next, sinusoidal fringes are projected, which are phase-shifted by $\pi/2$ each. From these images phase values are calculated pixel-wise [22]. The horizontal location of a homologous pair of points can then be obtained from the stack of binary and phase values. Along with the epipolar constraint [17], each pair can be identified unambiguously. Fig. 2 illustrates a measurement situation and the resulting point cloud rendered as a shaded triangle surface.

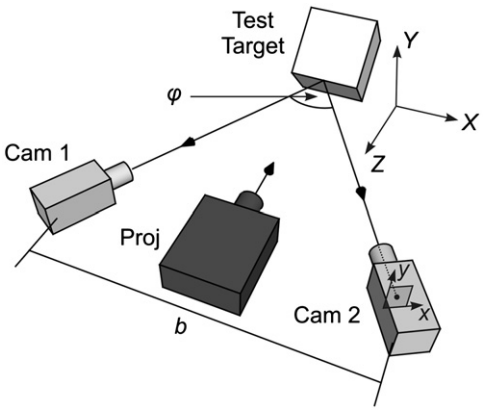

Fig. 1. Sketch of the fringe projecting topometric setup including the test target for the determination of the 3D transfer function. b denotes the basis length, i.e. the distance between the projection centers of the cameras, and φ denotes the triangulation angle. Object points in the world coordinate system $\{X, Y, Z\}$ are mapped into the image coordinate system $\{x, y\}$ on the camera sensor.

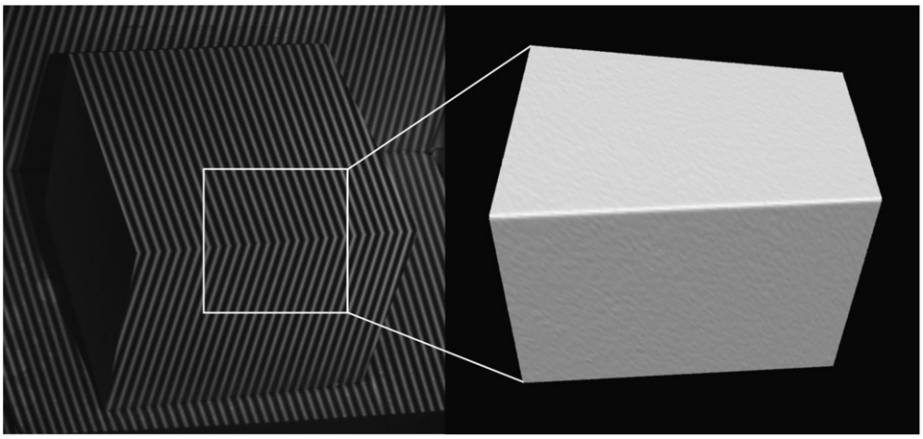

Fig. 2. Measurement image of the test target illuminated with a sinusoidal fringe pattern and a section of the respective triangulated point cloud.

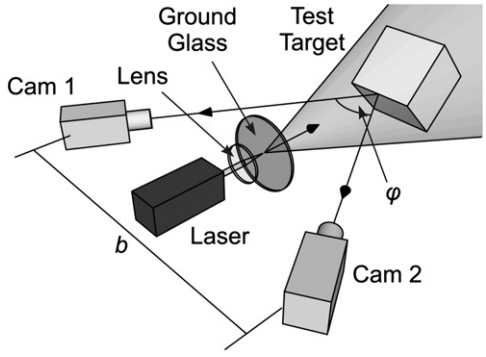

Fig. 3. Sketch of the speckle pattern projecting topometric setup including the test target for the determination of the 3D transfer function. b denotes the basis length and φ denotes the triangulation angle.

2.3. The speckle pattern projecting topometric system

The second topometric system differs from the one described in Section 2.2 only with respect to the technique used for finding homologous image points. A schematic of this setup is shown in Fig. 3. It utilizes a laser speckle pattern [23] projected onto the object's surface. The beam of a frequency doubled Nd:YAG CW laser with a wavelength of 532 nm and a maximum power of 21 mW (LCS-DTL-112A from Lasercompact, Moscow, Russia) is focused by a lens (f=80 mm) and passes a ground glass that generates a speckle pattern. Monochrome CCD cameras with 1280×960 pixels (IEEE 1394 interface) are used for recording.

While the automated determination of 3D coordinates with the fringe projection technique in our case requires 13 (stereo-) image pairs (see Section 2.2), the speckle pattern projection gets by with only one image pair. In this way, the measurement time is reduced to the single exposure time of the cameras, thus enhancing the reliability of non-stationary measurements. The pattern analysis is done by digital image correlation (DIC) as described in [24]. The method is mainly based on an algorithm proposed by Lu and Cary [25], which matches subsets of the two camera images by maximizing an adequate similarity measure. In order to simplify the correspondence analysis, the image pair is rectified in advance. This means that the image planes of both cameras are transformed in such a way that pairs of conjugate epipolar lines become collinear and in our case parallel to the horizontal image axis [26]. In the resulting rectified images, corresponding image points are located on the same horizontal line and the correspondence search can therefore be limited to a search along an image row.

Fig. 4 shows one of the recorded speckle images of the 3D TF test target and the resulting point cloud rendered as a shaded triangle surface.

2.4. Measurement of the modulation transfer function using a slanting edge technique

To estimate the (2D) MTF a technique is used, which is based on an approach presented by Buhr et al. [27]. There, the line spread function (LSF) is obtained as the numerical derivative of an edge spread function (ESF), which represents the system's response to an ideal black-to-white-transition (step response).

A large number (>100) of such transitions is used to obtain an oversampled ESF. The transitions are provided by the evaluation of an image of a slanted edge. This allows the determination of the MTF from a single measurement instead of evaluating multiple images of sinusoidal patterns with different frequencies.

The test target for the determination of the MTF is a printout from a laser printer displaying a pattern of alternating black and white stripes. Fig. 5 shows an image of this test target. It is slightly slanted with respect to the pixel grid of the recording camera. The distance between the target and the camera must be large enough to ensure that the blurring of the printout is not resolved by the cameras. So a laserprint target has sufficient accuracy for this purpose. In the present case, with a focal length of 12 mm, a distance of 60 cm is used. The oversampled ESF is extracted from a region of interest (ROI) within the image. The ROI is chosen according to the following criteria: the dark-to-bright-transition should be located approximately in the middle of the ROI. The width of the ROI should be at least 20 pixels as it defines the number of spatial frequencies where the MTF can be specified. The height of the ROI is just the number of rows after which the gray scale profile of the transition is displaced by one pixel due to the inclination of the test target. It should include a minimum of 15 pixels to ensure sufficient oversampling. Hence the inclination angle of the test target is not arbitrary and has to be adjusted to the chosen ROI height.

The gray scale values of the ROI are strung column by column as depicted in Fig. 6 to obtain the oversampled ESF. The ESF is then normalized by dividing by an averaged value of the bright part of the profile. Finally, the derivative of this signal is calculated to obtain the LSF. Due to the oversampling, the error caused by the numerical approximation of the derivative is negligible at the relevant low frequencies. A potential brightness inhomogeneity in the ESF may cause different values of the LSF at the beginning and the end of the block. In order to avoid an effect of this discontinuity on the spectrum, a window function is

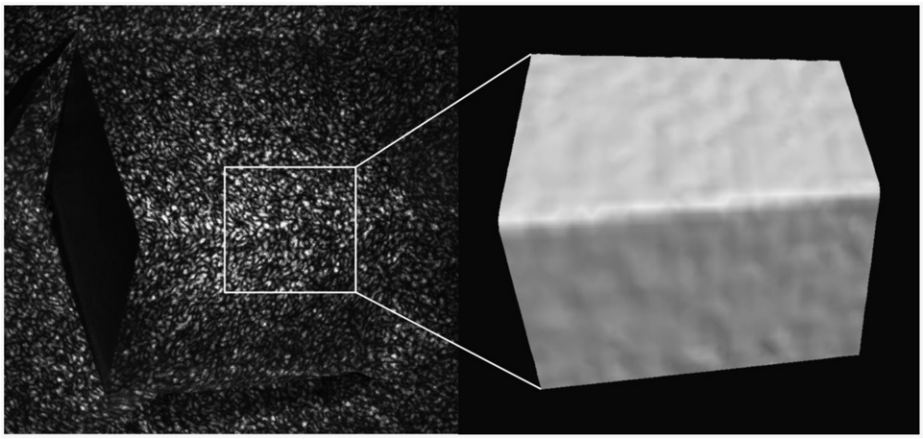

Fig. 4. Measurement image of the test target illuminated with a laser speckle pattern and a section of the respective triangulated point cloud.

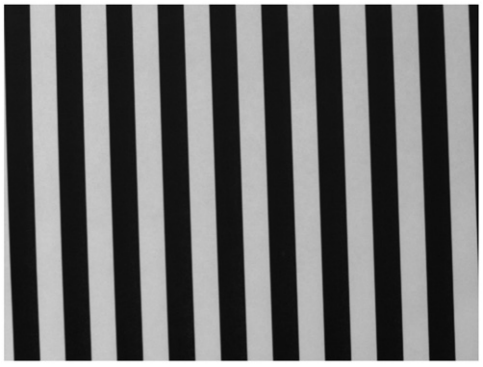

Fig. 5. Image of the slanted stripe pattern as it is used for the determination of the 2D modulation transfer function.

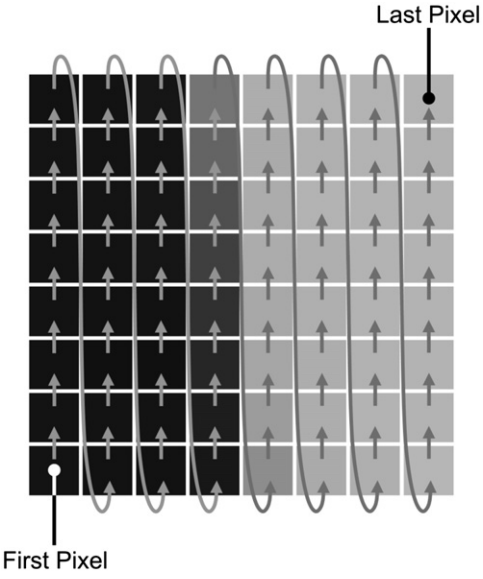

Fig. 6. Order of the pixels in a region of interest to build up the oversampled edge spread function.

applied to the LSF. Afterwards the MTF is calculated by applying the Fast Fourier Transform algorithm (FFT) to the windowed LSF and then taking the absolute value.

The ROI height is subject to a statistical spread, which is caused by the rounding to integer pixel coordinates as well as by variations of the inclination angle due to lens distortion. Thus, considering ROIs with one specific height would result in a MTF that is not representative for the investigated image section. To address this problem the MTF is determined as an average over all ROIs, which have at least the minimum height and which are found in the investigated section. Not only dark-to-bright-transitions but also bright-to-dark-transitions, after having rotated them through 180°, are included in the average. All these partial MTFs are weighted with the area of the respective ROIs.

2.5. Measurement of the 3D transfer function

The basic concept of a 2D transfer function analysis consists of determining the response of a system to a signal, which shows a sufficiently broad spatial frequency spectrum. The system is then characterized by the ratio of output and input frequency components [28]. Typically a pattern with a sharp edge is used (see Section 2.4) to obtain this broad spectrum. In order to translate this approach to the analysis of a 3D system, a precision-ground steel cuboid is used as a test target, which features a straight and sharp edge and two planar adjacent faces. The surface of the target is painted matte white to prevent specular reflections and achieve a homogeneous diffuse reflection. As shown in [15], the angle between the two adjacent faces has an effect on the measurement of the 3D transfer function. Thus, only measurements using a test target with the same angle are comparable. Here an angle of 90° is applied.

The starting point for the 3D TF analysis is the 3D point cloud delivered by a topometric measurement of the cuboid. To gain an oversampled profile, at least 100 edge profiles are extracted from the cloud and are superposed by parallel projection along the direction of the edge. The edge of the test target is slightly slanted against the pixel grid of the CCD sensor in order to avoid gaps in the superposed edge profile. Furthermore, the edge has to be oriented towards the cameras as shown in Fig. 1.

The obtained two-dimensional oversampled edge profile is then prepared for a Fourier analysis. It is symmetrically cropped and its bisecting line is aligned parallel to the ordinate. Furthermore, the profile is periodically continued by appending a version of it, which is reflected along the x-axis. In this way it is ensured that the two extrema are the only high-frequency features in the profile. Fig. 7a shows the result of these operations.

Since the x-coordinates are not equidistant, the profile is sampled along the x-axis at a rate of at least four times the Nyquist frequency of the signal. In the absence of an equally spaced grid, the Nyquist frequency $\xi_{Nyquist}$ is estimated as half the reciprocal of the mean distance $\overline{d}_{NN}$ of nearest neighbors in the 3D

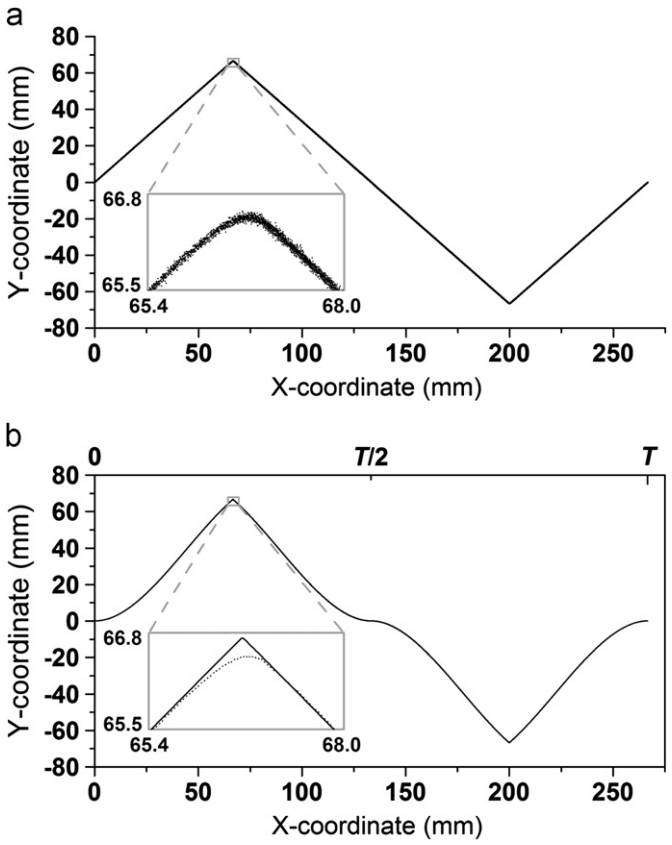

Fig. 7. (a) Periodically continued, oversampled edge profile. (b) Resampled edge profile and the perfectly sharp edge profile, both after the application of the window function. The insets in both plots show detailed enlargements of the left peak.

point cloud:

$$\xi_{Nyquist} = \frac{1}{2\,\bar{d}_{NN}}. \tag{4}$$

Next, the undistorted input signal has to be determined, which in our case is represented by the (supposedly perfectly sharp) edge profile of the cuboid. It is obtained by fitting straight lines to the slopes of the measured profile.

Finally, both halves of the measured and the input edge profile are separately multiplied by a Welch window in order to inhibit continuity errors between the profiles and their periodic continuations. Both signals are depicted in Fig. 7b.

Except for numerical errors, the signals satisfy the equation

$$f(x) = -f\left(x+\tfrac{T}{2}\right), \tag{5}$$

where T denotes the period length (see Fig. 7). Thus, the even coefficients in the spectrum are approximately zero. In order to enable the following division, only the odd coefficients, labeled with the index o, are taken into account. Moreover, the profiles are real-valued and odd except for numerical errors. Thus, the real parts of the spectra are negligible and only the imaginary parts of the odd coefficients need to be included. The 3D TF $H(\xi_o)$ is then given by

$$H(\xi_o) = \frac{\mathrm{Im}_o[FFT(q(x))]}{\mathrm{Im}_o[FFT(p(x))]}. \tag{6}$$

where ξ_o denotes the spatial frequency, q the resampled edge profile and p the perfect edge profile, both after the application of the window function. The 3D resolution in this case is defined as the spatial frequency limit where H drops beneath a given value.

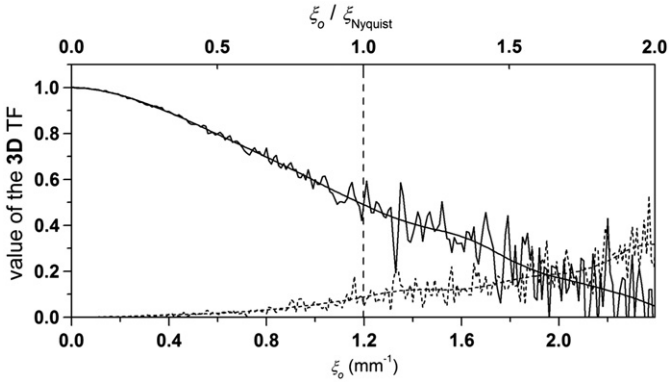

Fig. 8. Mean value (solid lines) and standard deviation (dashed lines) of the 3D transfer function, each with a B-spline-fit.

3. Experimental results and discussion

3.1. Reproducibility of the measurement of the 3D transfer function

In order to define the frequency limit used for characterizing the 3D resolution investigations on the reproducibility of the 3D TF measurement are carried out.

The fringe projection approach described in Section 2.2 is used for these measurements. In the present case CCD cameras of the type DMK 41BF02 by Imaging Source GmbH, Bremen, Germany, with 1280×960 pixels and 12 mm 1:1.4 lenses by Pentax are employed. The f-number is set to 5.6. For the measurement, a symmetric convergent setup (Fig. 1) is chosen meaning that the optical axes are converging and aligned in the same angle to the camera basis ($b = 44$ cm). The triangulation angle is $\varphi = 36^\circ$.

Utilizing the method described in Section 2.5, five measurements are performed, after each of which the test target is rotated slightly. From the five resulting 3D transfer functions, the mean value and the standard deviation are calculated. Both curves are smoothed by B-spline-fits. Fig. 8 shows H as a function of the spatial frequency ξ_o. The upper horizontal axis of the plot shows the spatial frequency normalized to the Nyquist frequency $\xi_{Nyquist}$, which is set to the average of the estimated Nyquist frequencies (see (4)) of all five measurements. $\xi_{Nyquist}$ amounts to about $1.2\ \mathrm{mm}^{-1}$ and is marked with a vertical dotted line. Since the spread of H increases with the spatial frequency, the frequency at which it drops to 0.6 is chosen as an indicator of the 3D resolution. For most cases this value is found within the range where H has its steepest slope. At the same time the standard deviation of H is still smaller than its mean value. In the following, this parameter will be used to quantify 3D resolution.

3.2. Comparison of 2D and 3D resolutions using low-pass filtered images for point cloud acquisition

In this section the influence of the camera image resolution on the 3D resolution of the measured point cloud is investigated. Five measurements are performed as described in Section 3.1. The calibration and the experimental setup are maintained except for a slight rotation of the test target between the measurements in order to determine the spread of H. First the obtained measurement data are evaluated in their original form and then with varying low-pass filtered camera images in order to simulate lower 2D resolutions. The applied low-pass filters are Butterworth filters of second order with eight different cut-off-frequencies between 330 and 125 pixel^{-1} at an image size of 1024×768 pixels. This filter type is chosen because its gain function shows no ripple.

The images are captured with monochrome cameras of the type Sony XCD-X700 with a pixel size of 6.25×6.25 µm and 12 mm 1:1.2 lenses (Cosmicar/Pentax) using an f-number of 5.6. The exposure time is adjusted to 1/16 s in order to avoid flickering caused by the color wheel of the projector. The camera basis is $b=43$ cm and the triangulation angle $\varphi=40^\circ$.

In addition to the 3D TF measurements, the 2D MTFs are determined from the inner sector of the original images as well as the eight filtered versions as explained in Section 2.4. This inner sector is defined as a circle of radius 192 pixels in the image center and contains the edge of the test target during the 3D measurement.

Fig. 9 shows the retrieved values of the 2D MTF with respect to the spatial frequency in the image plane (camera sensor). The 2D resolution is defined as the frequency where the 2D MTF drops to 0.5. Fig. 10 depicts the confidence belts of the B-spline-smoothed mean values and standard deviations (error bars) of the 3D TFs for all nine cases. Fig. 11 shows the plot of the 2D and 3D uncertainties that are determined by calculating the reciprocals of the 2D and 3D resolutions in Figs. 9 and 10, respectively. For a better comparability, the 2D uncertainties are converted to mm by dividing them by the reproduction scale of 1024 pixels per 265 mm.

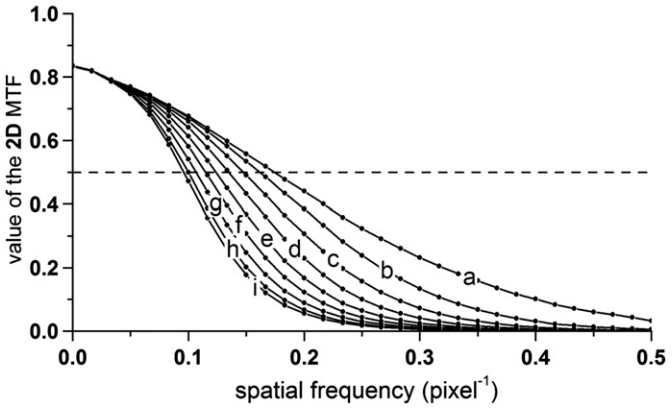

Fig. 9. 2D modulation transfer functions of the inner sector of the unfiltered image (a) and the images filtered with Butterworth low-pass-filters (b–i). The cut-off-frequencies of the filters are 330 (b), 251 (c), 208 (d), 180 (e), 160 (f), 144 (g), 132 (h) and 125 pixel^{-1} (i). The dashed line marks the level where the 2D resolution is defined.

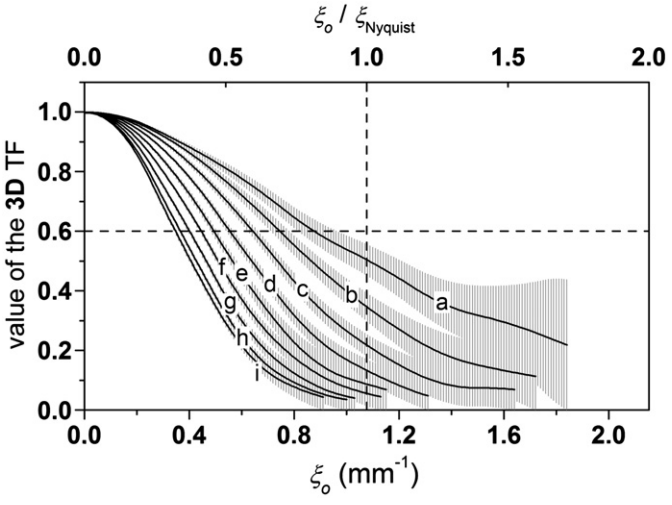

Fig. 10. Confidence belts of the 3D transfer functions of 3D coordinate measurements using the unfiltered (a) and filtered images (b–i). They are established by the B-spline-smoothed mean values and standard deviations over five measurements. The cut-off-frequencies of the filters are denoted in Fig. 9. The 3D resolutions are those frequencies where the curves cross the horizontal dashed line, which marks the 3D transfer function value 0.6.

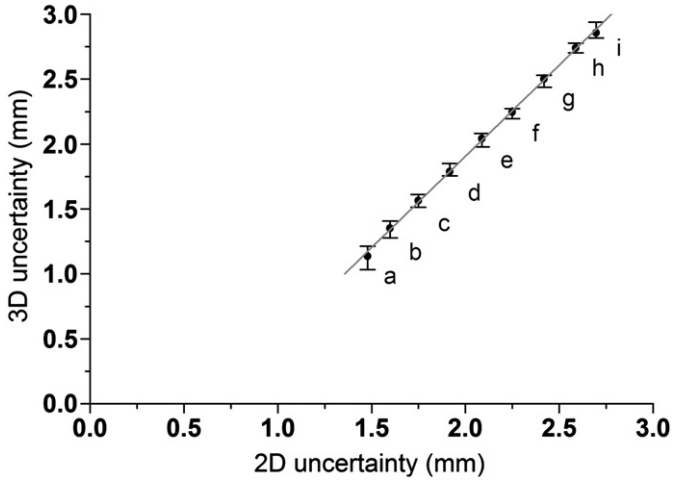

Fig. 11. Plot of the 3D uncertainty vs. the 2D uncertainty. The numbering (a–i) is the same as in Figs. 9 and 10.

The linear fit in Fig. 11 shows that the experimental data are in agreement with the expectations of the coordinate mean errors of the stereo normal case (2), (3), which is an approximation of the actual setup (see Fig. 1). The calibration error, here given by the errors of f and b, is assumed to be small and thus neglected. Furthermore, neglecting the first summand in (3), which is small for small x_1 near the image center, and replacing the image-related accuracies σ_x and σ_{px} by a general image accuracy σ_i results in the proportionality:

$$\sigma_{X,Y,Z} \sim \sigma_i. \tag{7}$$

The offset of the straight line in Fig. 11 from the origin has its source in the chosen definition of the 2D and 3D (see Section 2.5) resolutions.

3.3. Influence of the triangulation angle on the 3D resolution

For the investigated experimental setup the triangulation angle φ is defined as the angle between the optical axes of the two involved cameras (see Fig. 1). It represents a mean value of the individual triangulation angles of single 3D points in the evaluated point cloud as the test target for the determination of the 3D TF is placed centrally in the camera images. Thus, the relevant image points are situated near to the principal point.

The used setup and devices are the same as in Section 3.2. The triangulation angle φ is varied in a range from 21° to 71° by increasing the distance between the cameras from 24 cm to 80 cm without changing the distance between the test target and the camera lenses. Two series of measurements are presented here, the first covering triangulation angles from 21° to 29°, the second covering 32° to 71°. Within each series the internal camera parameters (focal lengths, positions of the principal points, lens distortion parameters) are calibrated once while the external parameters (position and orientation of the cameras) of course have to be updated for each angle.

In analogy to the measurement described in Section 3.1, in five measurements per triangulation angle mean and standard deviation values of the 3D transfer function H are determined. From this curves the 3D resolutions are extracted and depicted in Fig. 12. The corresponding triangulation angles are calculated from the rotation matrices (see (1)), which are determined during the calibration progress.

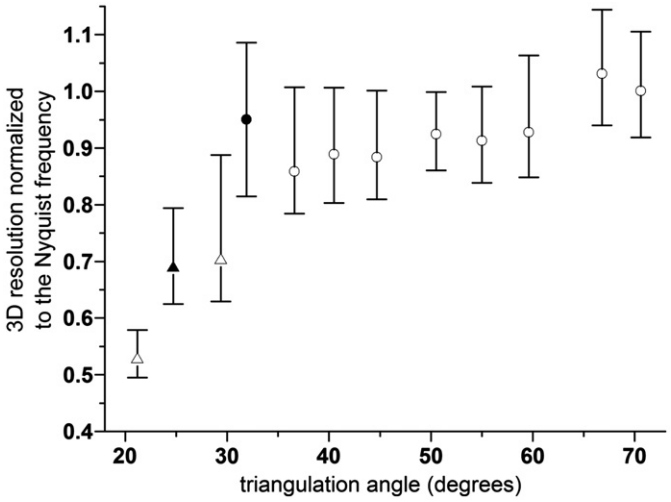

Fig. 12. 3D resolution normalized to the Nyquist frequency with respect to the triangulation angle. Two series of measurements are displayed, the first denoted by triangles and the second by circles. Within each series only the calibration of the position and the orientation of the cameras are renewed per angle while the other parameters are retained. The filled symbols mark those angles (25° and 32°) where a complete calibration of all parameters is performed.

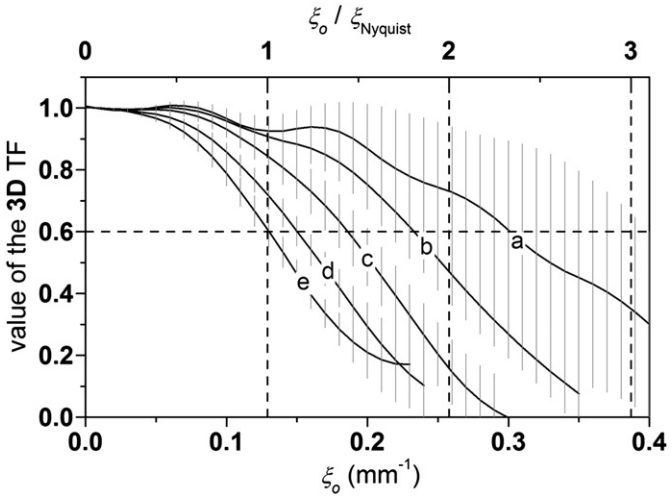

Fig. 13. Confidence belts of the 3D transfer functions of 3D coordinate measurements using digital image correlation of projected speckle patterns. The subset sizes are 15 (a), 21 (b), 27 (c), 33 (d) and 39 pixels (e).

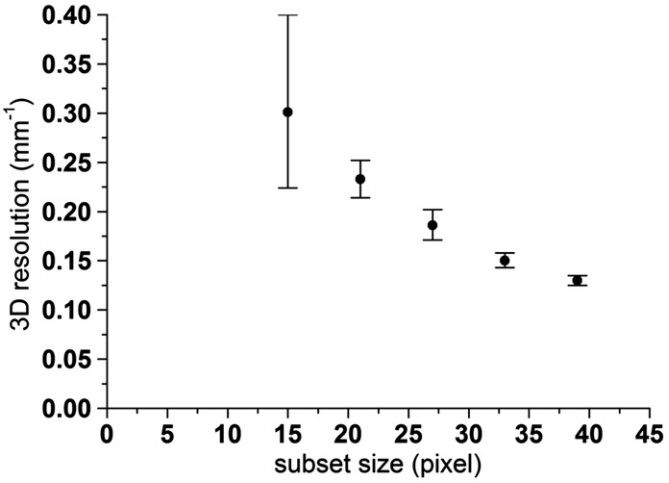

Fig. 14. 3D resolution with respect to the subset size.

The 3D resolution shows a fundamental dependency on the point density of the cloud, since fewer points can reproduce less details of the regarded surface. The point density depends on the angle between the optical axis and the surface at a constant camera-to-subject distance and is maximal for a perpendicular view. Therefore, smaller triangulation angles result in higher point densities. To account for this influence, the 3D resolutions are normalized to the respective Nyquist frequencies.

As Fig. 12 illustrates, the 3D resolution increases with the triangulation angle, and the increase is especially pronounced in the range up to 32°. A consideration of the probability density function of a reconstructed 3D point [17] gives a description of the triangulation error, which affects the 3D resolution, and qualitatively predicts this behavior. The angles at which the complete calibration is performed (filled symbols in Fig. 12) show a significantly higher 3D resolution than the others. This can be an indication that the calibration is more accurate when the complete set of parameters is calibrated together. This is plausible since the calibration technique includes an optimization over all parameters [18], which is skipped if only the camera position and orientation parameters are updated.

3.4. *Influence of the subset size in digital correlation of speckle patterns on the 3D resolution*

The speckle pattern projecting topometric system (Fig. 3) differs from the fringe projection system mainly by the way in which corresponding (homologous) image points are detected in the stereo image pairs. A crucial parameter here is the size of the image subsets, which are used during the correlation process. So the influence of this parameter is investigated as an example with the presented approach. The setup involves the same (monochrome) CCD cameras and lenses (f/5.6) as in Section 3.1. It is symmetrically convergent with a triangulation angle of 35° and a camera basis of 37 cm. The speckle size is adjusted to about 5 pixels. A detailed description of the determination of the speckle size is presented in [24] and is based on the autocorrelation function of the speckle pattern [29]. The image subsets used in the DIC algorithm are squares with edge lengths of 15, 21, 27, 33 and 39 pixels.

The obtained (smoothed) 3D TFs and standard deviations are depicted in Fig. 13. Fig. 14 shows the extracted 3D resolutions. The 3D resolution as well as its uncertainty decrease with increasing subset sizes. Thus, larger subsets have a smoothing effect on the point cloud. On one hand this reduces noise, on the other hand, high-frequency features of the object are suppressed and accordingly the 3D resolution. A further measurement using a subset size of only 9 pixels could not be evaluated due to the noise.

The Nyquist frequency gives an indication whether the point density of the cloud is sufficient to exploit the 3D resolution of the system. Here, every fifth pixel in each direction of the main camera's image is evaluated to obtain a 3D point because the DIC algorithm is very time consuming. The resulting Nyquist frequency just matches the 3D resolution for a subset size of 39 pixels as Fig. 13 shows. For smaller subset sizes even lower point densities would be sufficient.

4. Conclusions

A novel approach to determine the resolution of topometric 3D measurement systems by a 3D transfer function has been applied to characterize and compare the accuracy of two such systems based on fringe and laser speckle projection. Both systems use the

same photogrammetric methods for calculating 3D coordinates from image pairs while utilizing different techniques to identify homologous points through evaluation of projected patterns. As a consequence, the measurement setups appear to be good candidates for a direct comparison. The 3D resolution calculated with the proposed approach then has been evaluated in relation to the 2D resolution of the processed camera images. Furthermore, the dependencies of the 3D resolution on the triangulation angle and on the size of the correlation window have been investigated.

The 3D resolution turns out to be a reliable overall quality criterion of a 3D point cloud that is influenced by several effects: it comprises lateral and axial measurement errors affected by the uncertainty of the setup's calibration parameters as well as the uncertainty of the identification of homologous image points. The latter is influenced for instance by the 2D image resolution. In Section 3.2 it has been illustrated that the 3D uncertainty increases with the 2D uncertainty almost linearly. The results of Section 3.3 demonstrate that larger triangulation angles yield higher 3D resolutions with a pronounced increase for angles up to 32°. When comparing typical measuring setups of the two topometric systems, the fringe projection technique (Section 3.3, triangulation angle: 36.6°) shows a 3D resolution which is about 3.5 times the 3D resolution of the speckle pattern projecting system (Section 3.4, subset size: 21 pixels). As it is shown in Section 3.4, larger subset sizes of the DIC algorithm result in lower 3D resolutions.

The definition of the 3D resolution established in Section 3.1 appears to be a reasonable criterion when taking into consideration the uncertainty of the 3D TF. Other experiments not described here suggest that the 3D resolution, which is achievable in praxis, is underestimated by the definition chosen here. Nevertheless, it has been demonstrated that the method of 3D TF determination is suitable for a simple comparison of the 3D resolution of two different 3D sensors. In general it is applicable to all measuring systems that produce a point cloud as it is capable of measuring 3D resolutions in a wide range. The used test target is easy to manufacture and therefore cheap.

Acknowledgment

The presented work has been carried out within the frame of an interdisciplinary project in which the computer aided construction of facial prostheses based on optically acquired data is investigated. Financial support by the Deutsche Krebshilfe (German Cancer Aid) is gratefully acknowledged.

References

[1] Gruen A, Kahmen A. Optical 3-D measurement techniques: IV. Karlsruhe: Wichmann Verlag; 1997.
[2] Bischoff G, Böröcz Z, Proll C, Kleinheinz J, von Bally G, Dirksen D. Modular optical topometric sensor for 3D acquisition of human body surfaces and long-term monitoring of variations. Biomed Tech 2007;52:284–9.
[3] Westhäuser M, Bischoff G, Böröcz Z, Kleinheinz J, von Bally G, Dirksen D. Optimizing color reproduction of a topometric measurement system for medical applications. Med Eng Phys 2008;30:1065–70.
[4] Frankowski G, Chen M, Huth T. Real-time 3D shape measurement with digital stripe projection by Texas instruments micromirror devices DMD. Proc SPIE 2000;3958:90–105.
[5] Notni G, Kühmstedt P. German patent DE 196 33 686 C2. Deutsches Patentamt; 19 February 1998.
[6] Gorthi SS, Rastogi P. Fringe projection techniques: whither we are? Opt Lasers Eng 2010;48:133–40.
[7] Notni GH, Notni G. Digital Fringe projection in 3D shape measurement—an error analysis. Proc SPIE 2003;5144:372–80.
[8] Guo H, He H, Chen M. Gamma correction for digital fringe projection profilometry. Appl Opt 2004;43:2906–14.
[9] OpenCV. Open source computer vision library, 〈http://opencv.willowgarage.com/wiki/〉; 1 September 2011.
[10] Brakhage P, Notni G, Kowarschik R. Image aberrations in optical three-dimensional measurement systems with fringe projection. Appl Opt 2004;43:3217–23.
[11] Bräuer-Burchardt C, Palme M, Kühmstedt P, Notni G. Optimised projection lens for the use in digital fringe projection. In: Osten W, editor. Proceedings of the fifth international workshop on automatic processing of fringe patterns. Berlin: Springer; 2005. p. 676–81.
[12] Notni G, Schreiber W, Heinze M, Notni G. Flexible autocalibrating full-body 3D measurement system using digital light projection. Proc SPIE 1999;3824:79–87.
[13] Huang PS, Hu Q, Chiang F-P. Error compensation for a three-dimensional shape measurement system. Opt Eng 2003;42:482–6.
[14] Steger C, Ulrich M, Wiedemann C. Machine vision algorithms and applications. Weinheim: Wiley-VCH; 2008.
[15] Goesele M, Fuchs C, Seidel H-P. Accuracy of 3D range scanners by measurement of the slanted edge modulation transfer function. In: Proceedings of the fourth international conference on 3-D digital imaging and modeling, vol. 37. IEEE Computer Society; 2003.
[16] Reichenbach SE, Park SK, Narayanswamy R. Characterizing digital image acquisition devices. Opt Eng 1991;30:170.
[17] Hartley R, Zisserman A. Multiple view geometry in computer vision. Cambridge: Cambridge University Press; 2003.
[18] Zhang Z. A flexible new technique for camera calibration. Microsoft Research Technical Report MSR-TR-98-71; 1998.
[19] Faugeras O. Three-dimensional computer vision—a geometric viewpoint. Cambridge: The MIT Press; 1993.
[20] Kraus K. Photogrammetry—geometry from images and laser scans. Berlin: de Gruyter; 2007.
[21] Srinivasan V, Liu HC, Halioua M. Automated phase-measuring profilometry of 3-D diffuse objects. Appl Opt 1984;23:3105.
[22] Creath K. Phase-measurement interferometry techniques. Prog Opt 1988;26:349.
[23] Dainty C, editor. Laser speckle and related phenomena. Berlin: Springer Verlag; 1984.
[24] Dekiff M, Berssenbrügge P, Kemper B, Denz C, Dirksen D. Three-dimensional data acquisition by digital correlation of projected speckle patterns. Appl Phys B 2010;99:449.
[25] Lu H, Cary PD. Deformation measurements by digital image correlation: Implementation of a second-order displacement gradient. Exp Mech 2000;40:393.
[26] Fusiello A, Trucco E, Verri A. A compact algorithm for rectification of stereo pairs. Mach Vision Appl 2000;12:16.
[27] Buhr E, Günther-Kohfahl S, Neitzel U. Simple method for modulation transfer function determination of digital imaging detectors from edge images. Proc SPIE 2003;5030:877.
[28] Goodman JW. Introduction to Fourier optics. Roberts & Co., Englewood; 2005.
[29] Goodman JW. Statistical properties of laser speckle patterns. In: Dainty JC, editor. Laser speckle and related phenomena. Berlin: Springer; 1984. p. 9–75.